Raman spectroscopy of shear and layer breathing modes in multilayer MoS_2

X. Zhang,[1] W. P. Han,[1] J. B. Wu,[1] S. Milana,[1,2] Y. Lu,[1] Q. Q. Li,[1] A. C. Ferrari,[2,*] and P. H. Tan[1,†]

[1]*State Key Laboratory of Superlattices and Microstructures, Institute of Semiconductors, Chinese Academy of Sciences, Beijing 100083, China*

[2]*Cambridge Graphene Centre, University of Cambridge, Cambridge CB3 OFA, United Kingdom*

(Received 23 January 2013; published 13 March 2013)

We study by Raman scattering the shear and layer breathing modes in multilayer MoS_2. These are identified by polarization measurements and symmetry analysis. Their positions change significantly with the number of layers, with different scaling for odd and even layers. A chain model can explain the results, with general applicability to any layered material, allowing a reliable diagnostic of their thickness.

DOI: 10.1103/PhysRevB.87.115413 PACS number(s): 63.10.+a, 63.20.dk, 71.15.Mb

I. INTRODUCTION

The fast progress of graphene research, fueled by the unique properties of this two-dimensional (2d) material, paved the way to experiments on other 2d crystals.[1–3] There are several layered materials (LMs), studied in the bulk,[4] retaining their stability down to a single monolayer, and whose properties are complementary to those of graphene. Transition metal oxides[5] and metal dichalcogenides have a layered structure.[4] Atoms within each layer are held together by covalent bonds, while van der Waals interactions keep the layers together.[4] LMs include a large number of systems with interesting properties.[4] For example, $NiTe_2$ and VSe_2 are semimetals;[4] WS_2,[6] WSe_2,[7] MoS_2,[8] $MoSe_2$, $MoTe_2$, TaS_2,[9] $RhTe_2$ and $PdTe_2$ are semiconductors;[4] h-BN, and HfS_2 are insulators; NbS_2, $NbSe_2$,[10] $NbTe_2$, and $TaSe_2$ are superconductors;[4] Bi_2Se_3[11] and Bi_2Te_3[11] show thermoelectric properties[4] and may be topological insulators.[12] Similar to graphite and graphene, the LM properties are a function of the number of layers (N). The combinations of such 2d crystals in 3d stacks could offer huge opportunities in designing the functionalities of such heterostructures.[1,2] One could combine conductive, insulating, superconducting and magnetic 2d materials in one stack with atomic precision, fine tuning the performance of the resulting material,[1] the functionality being embedded in the design of such heterostructures.[1]

Amongst these LMs, MoS_2 is a subject of intense research because of its electronic[13] and optical properties,[14] such as strong photoluminescence (PL),[14,15] electroluminescence,[16] controllable valley and spin polarization.[17–19] A single layer MoS_2 (1L-MoS_2) consists of two planes of hexagonally arranged S atoms linked to a hexagonal plane of Mo atoms via covalent bonds.[14,20–23] In the bulk, individual MoS_2 layers are held together by weak van der Waals forces.[20–23] This property has been exploited in lubrication technology[24] and, more recently, enabled the isolation of 1L-MoS_2.[13–15,25] While bulk MoS_2 is a semiconductor with a 1.3-eV indirect band gap,[26] 1L-MoS_2 has a 1.8-eV direct band gap.[14,15] The absence of interlayer coupling of electronic states at the Γ point of the Brillouin zone in 1L-MoS_2[15,27] results in strong absorption and PL bands at $\sim$1.8 eV (680 nm).[14,15] 1L-MoS_2 field effect transistors (FETs) show both unipolar[13] and ambipolar[28] transport, with high mobilities and on-off ratios.[29,30] 1L-MoS_2 is also a promising candidate for novel optoelectronic devices,[16] such as photodetectors[31–33] and light-emitting devices operating in the visible range.[16]

Raman spectroscopy is the prime nondestructive characterization tool for carbon materials,[34,35] in particular graphite,[35–38] single,[35,39] and multilayer[35,39] graphene. The Raman spectrum of graphene consists of two fundamentally different sets of peaks. Those, such as D, G, 2D, etc., due to in-plane vibrations,[34–36] and others, such as the shear (C)[40] and layer breathing (LB) modes (LBMs),[41–43] due to relative motions of the planes themselves, either perpendicular or parallel to their normal. Albeit being an in-plane mode, the 2D peak is sensitive to N since the resonant Raman mechanism that gives rise to it is closely linked to the details of the electronic band structure,[35,39,44] the latter changing with N,[45,46] and the layers relative orientation.[44] On the other hand, the C modes and LBMs are a direct probe of N,[40–42] since the vibrations themselves are out of plane, thus directly sensitive to N. The success of Raman scattering in characterizing graphene prompted the community to extend this technique to other LMs, from bulk to monolayer.[40,47–52] For example, the Raman spectrum of bulk MoS_2 consists of two main peaks at $\sim$382, 407 cm^{-1}.[53,54] These are assigned to E^1_{2g} (in-plane vibration) and A_{1g} (out of plane vibration) modes.[53,54] The E^1_{2g} red shifts, while the A_{1g} blue shifts with increasing N.[49,55] The E^1_{2g} and A_{1g} modes have opposite trends when going from bulk MoS_2 to 1L-MoS_2, so that their difference can be used to monitor N.[49] The E^1_{2g} shift with N may be attributed to stacking-induced structure changes, or long-range Coulombic interlayer interactions,[49,55] while the A_{1g} shift is due to increasing restoring forces as additional layers are added.[49,55] Further work is still needed to fully clarify and assign these trends.

Our focus here is on the C and LB modes that appear in the low-frequency region in the various LMs.[56] These have been extensively studied in multilayer graphene.[40–42,57] Unlike graphite and graphene, most LMs consist of more than one atomic element. For example, each MoS_2 layer contains one Mo plane sandwiched by two S planes, while Bi_2Se_3 contains two Bi and three Se planes. This makes their lattice dynamics more complex than multilayer graphene, starting from the symmetry and force constants. Even NL-MoS_2 (ENL-MoS_2) belong to point group D_{6h} with inversion symmetry, while odd NL-MoS_2 (ONL-MoS_2) correspond to D_{3h} without inversion symmetry.[58] There are a few reports on C and LBMs in LMs other than graphene. Reference 59 reported them in bulk samples as: $\sim$21.5 cm^{-1} (C), 32.5 cm^{-1}(C), $\sim$50 cm^{-1}(LBM) for As_2Se_3 at 15 K; $\sim$27 cm^{-1}(C), 38 cm^{-1}(C), $\sim$60 cm^{-1}(LBM) for As_2S_3 at

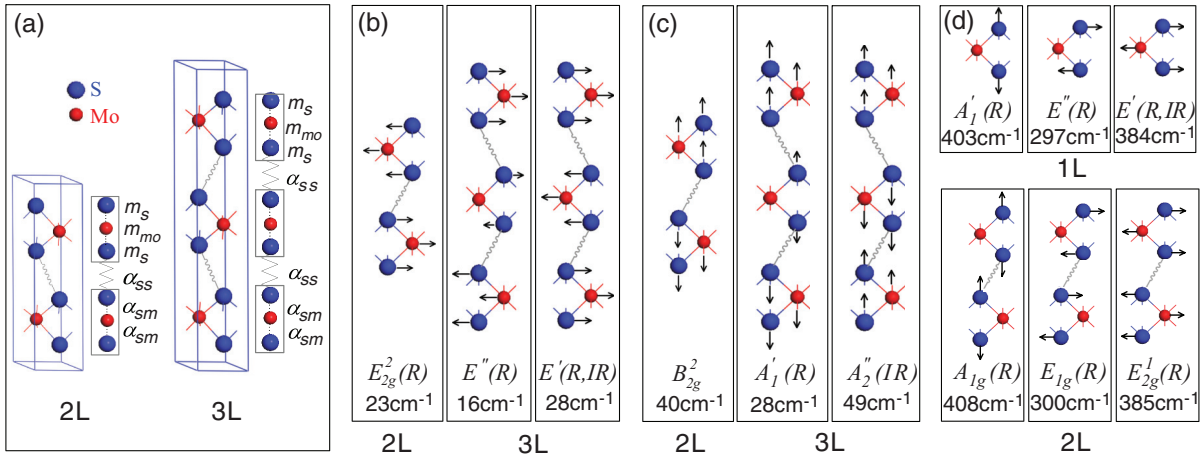

FIG. 1. (Color online) (a) Lattice structure and linear chain models of 2 and 3L-MoS_2. Inversion symmetry applies to 2, not 3L-MoS_2. (b) C modes and (c) LBMs in 2 and 3L-MoS_2. (d) High-frequency optical vibration modes for 1 and 2L-MoS_2. The symbol under each mode is its irreducible representation. R or IR indicate if the mode is Raman, or infrared active, or both. The theoretical results based on the diatomic chain model are also indicated.

15 K; ~34 cm^{-1} (C), ~56 cm^{-1} (LBM) for MoS_2; ~22 cm^{-1} (C) for GaS; ~56 cm^{-1} (C) for GaSe. Only Refs. 51 and 52 reported some of these for non-bulk samples. In particular, Ref. 51 studied the Raman spectrum of one shear mode for 2, 3, 5, 6, and 10L-MoS_2. Reference 52 observed only one set of C and LB modes for 2 to 6L-MoS_2 and 9L-MoS_2. Both did not consider the symmetry difference between ONL-MoS_2 and ENL-MoS_2, e.g., they assigned the C mode in ONL MoS_2 as E^2_{2g}, but, as we show later, this is instead E'. Reference 51 suggested that the scaling rule of the C mode in multilayer graphene[40] cannot be extended to few-layer MoS_2, opposite to the results presented in Ref. 52. Reference 52 wrote that LBMs scale as $1/N$, as predicted by Ref. 60 with an assumption of strong coupling between layers and substrate. However, it is not clear whether such strong coupling actually exists. Furthermore, even though LBMs are optical modes, an acoustic atomic displacement for such modes was presented in Fig. 1(b) of Ref. 52, with no symmetry analysis. Therefore, all symmetries, force constants, possible role of interactions between layers and substrate, and mode scaling with N still need to be fully understood. More importantly, it would be desirable to establish a general model to describe the evolution of C and LB modes with N in any LMs, not just MoS_2.

Here we report the shear and layer breathing modes for NL-MoS_2 up to 19L-MoS_2, and bulk MoS_2. We identify several groups of modes with frequencies dependent on N. ONL-MoS_2 and ENL-MoS_2 show different scaling with N, due to different symmetry. A chain model can account for the observed trends, and can be extended to other LMs.

II. RESULTS AND DISCUSSION

NL-MoS_2 samples are produced from bulk MoS_2 (SPI Supplies) by mechanical exfoliation, following a similar procedure to that used for graphene samples.[2,61] NL-MoS_2 are supported on a Si wafer with 93-nm SiO_2, which is used as substrate in order to make the samples optically visible. The layer thickness is determined by optical contrast[62] and atomic force microscopy.[55] Raman measurements are performed using a Jobin-Yvon HR800 system equipped with a liquid nitrogen cooled charge-coupled detector. The excitation wavelength is 532 nm from a diode-pumped solid-state laser. A power ~0.23 mW is used to avoid sample heating. The laser plasma lines are removed using a BragGrate bandpass filter (OptiGrate Corp), as these would appear in the same spectral range as the modes of interest. The Rayleigh line is suppressed using four BragGrate notch filters with an optical density 3 and a spectral bandwidth ~5–10 cm^{-1}. This configuration is similar to that used in Ref. 40 for multilayer graphene. The spectral resolution is ~0.6 cm^{-1}, as estimated from the full width at half maximum (FWHM) of the Rayleigh peak.

Bulk MoS_2 and 2L-MoS_2 belong to the space group $P6_3/_{mmc}$ (point group D_{6h}),[63] with unit cell consisting of two Mo atoms in sites with point group D_{3h}, and four S atoms in sites with point group C_{3v},[53] as shown in Fig. 1(a). There are 18 normal vibration modes.[63] The factor group of bulk and 2L-MoS_2 at Γ is D_{6h}, the same as the point group.[64] The atoms site groups are a subgroup of the crystal factor group.[64] The correlation[53] of the Mo site group D_{3h}, S site group C_{3v}, and factor group D_{6h} allows one to derive the following irreducible representations for the 18 normal vibration modes at Γ:[53,65]
$\Gamma = A_{1g} + 2A_{2u} + 2B_{2g} + B_{1u} + E_{1g} + 2E_{1u} + 2E_{2g} + E_{2u}$,
with A_{2u} and E_{1u} translational acoustic modes, A_{1g}, E_{1g}, and E_{2g} Raman active, A_{2u} and E_{1u} infrared (IR) active. The E_{1g} and A_{1g} modes and one of the doubly degenerate E_{2g} modes, E^1_{2g}, as shown in Fig. 1(d) for 2L and bulk MoS_2, give rise to Raman modes above 200 cm^{-1}.[49] Only A_{1g} (~408 cm^{-1} in bulk and ~405 cm^{-1} in 2L-MoS_2) and E^1_{2g} (~382 cm^{-1} in bulk and ~383 cm^{-1} in 2L-MoS_2) can be observed when the laser excitation is normal to the sample basal plane.[49] The other doubly degenerate E_{2g} mode, E^2_{2g}, and one B_{2g} mode, B^2_{2g}, are shear and LB modes.[53,54,66] E^2_{2g} corresponds to a rigid-layer displacement perpendicular to the c axis (C mode), while B^2_{2g} corresponds to rigid-layer displacements parallel to the c axis (LBM), as shown in Figs. 1(b) and 1(c) for 2L-MoS_2.

1L-MoS_2 has D_{3h} symmetry, with three atoms per unit cell.[63] The Γ phonons can be expressed by the irreducible

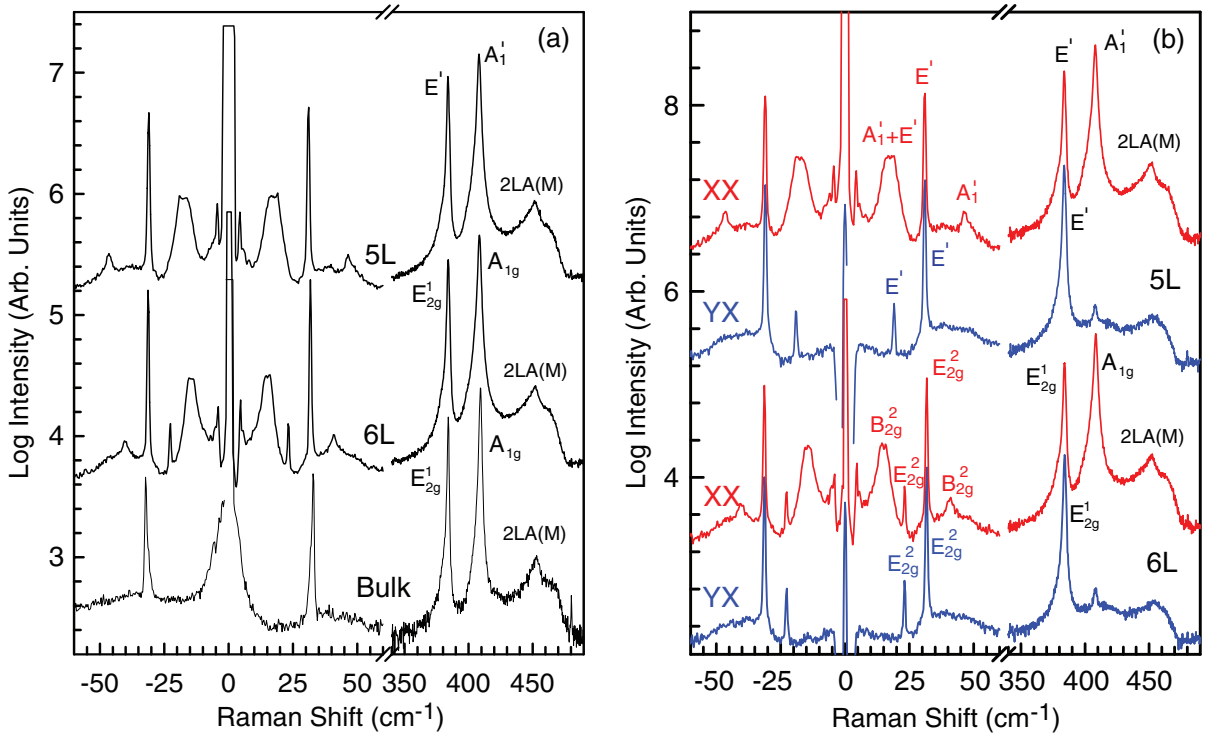

FIG. 2. (Color online) (a) Raman spectra of 5, 6L, and bulk MoS_2. (b) Raman spectra of 5 and 6L-MoS_2 measured for *XX* (red) and *YX* (blue) polarizations. The irreducible representation of each mode is indicated.

representation of D_{3h}:[63,65] $\Gamma = 2A_2'' + A_1' + 2E' + E''$, where A_2'' and E' are acoustic modes, A_2'' is IR active, A_1' and E'' are Raman active, and another E' is both Raman and IR active. The E' and A_1' modes, Fig. 1(d), were previously detected in the Raman spectra of 1L-MoS_2 at ~384 and ~403 cm^{-1}.[49] Of course, no rigid-layer vibrations can exist in 1L-MoS_2.

3L-MoS_2 has the same point group (D_{3h}) as 1L-MoS_2, with A_1' and A_2'' corresponding to LBMs, and E' and E'' being C modes, Figs. 1(b) and 1(c). ENL-MoS_2 belongs to point group D_{6h} (with inversion symmetry), while ONL-MoS_2 corresponds to D_{3h} (without inversion symmetry).[58] Therefore, it is convenient to denote each mode of *N*L-MoS_2 by the corresponding irreducible representation according to the their point group, and then determine if they are Raman or IR active, or inactive.

*N*L-MoS_2 has $9N - 3$ optical modes: $3N - 1$ are vibrations along the *c* axis, and $3N - 1$ are doubly degenerate in-plane vibrations. For rigid-layer vibrations, there are $N - 1$ LBMs along the *c* axis, and $N - 1$ doubly degenerate shear modes perpendicular to it. When *N* is even, there are 0 Raman active LBMs and $\frac{N}{2}$ doubly degenerate Raman active shear modes. When *N* is odd, $\frac{N-1}{2}$ LBMs and $N - 1$ doubly degenerate shear modes are Raman active. The interlayer distance in LMs is much larger than the in-plane bond length, e.g., in MoS_2 the interlayer distance is ~6.7 Å, while the in-plane bond length is ~3.2 Å.[67] Thus, the in-plane optical modes may not strongly depend on *N*. However, the interlayer coupling dominates the lattice dynamics of the rigid-layer vibrations, so that LB and shear modes will be very sensitive to *N*. For example, Fig. 2(a) shows the Raman spectra of 5, 6L, and bulk MoS_2. In the high-frequency region above 200 cm^{-1}, the E_{2g}^1 (~384 cm^{-1}), A_{1g} (~409 cm^{-1}), 2LA(M) (~453 cm^{-1}), and A_{2u} (~463 cm^{-1}) modes are detected both in bulk and 6L-MoS_2. Although the notation in 5L-MoS_2 is different from 6L and bulk MoS_2 because of the different crystal symmetry, the modes (E', A_1') are observed in 5L-MoS_2. The line shape and peak positions in the high-frequency region for 5L and 6L-MoS_2 are almost identical, both being similar to bulk MoS_2. In the low-frequency region below 100 cm^{-1}, there is only one Raman peak ~33 cm^{-1}, i.e., E_{2g}^2, in bulk MoS_2. However, as discussed above, there should exist six Raman active modes for 5L and three for 6L-MoS_2. Of these, four and three shear modes should be doubly degenerate for 5L and 6L-MoS_2, respectively. Experimentally, we observe three modes below 60 cm^{-1} in 5L and four modes in 6L-MoS_2, as for Fig. 2(a).

The LB (A_1') and C (E', E'') Raman tensors in ONL-MoS_2, and C (E_{2g}^2) Raman tensor in ENL-MoS_2 are[68,69]

$$A_1' \text{ (LB,ONL)}: \begin{bmatrix} a & 0 & 0 \\ 0 & a & 0 \\ 0 & 0 & b \end{bmatrix},$$

$$E' \text{ (C,ONL)}: \begin{bmatrix} 0 & d & 0 \\ d & 0 & 0 \\ 0 & 0 & 0 \end{bmatrix}, \begin{bmatrix} d & 0 & 0 \\ 0 & -d & 0 \\ 0 & 0 & 0 \end{bmatrix},$$

$$E'' \text{ (C,ONL)}: \begin{bmatrix} 0 & 0 & 0 \\ 0 & 0 & c \\ 0 & c & 0 \end{bmatrix}, \begin{bmatrix} 0 & 0 & -c \\ 0 & 0 & 0 \\ -c & 0 & 0 \end{bmatrix},$$

$$E_{2g}^2 \text{ (C,ENL)}: \begin{bmatrix} 0 & d & 0 \\ d & 0 & 0 \\ 0 & 0 & 0 \end{bmatrix}, \begin{bmatrix} d & 0 & 0 \\ 0 & -d & 0 \\ 0 & 0 & 0 \end{bmatrix}.$$

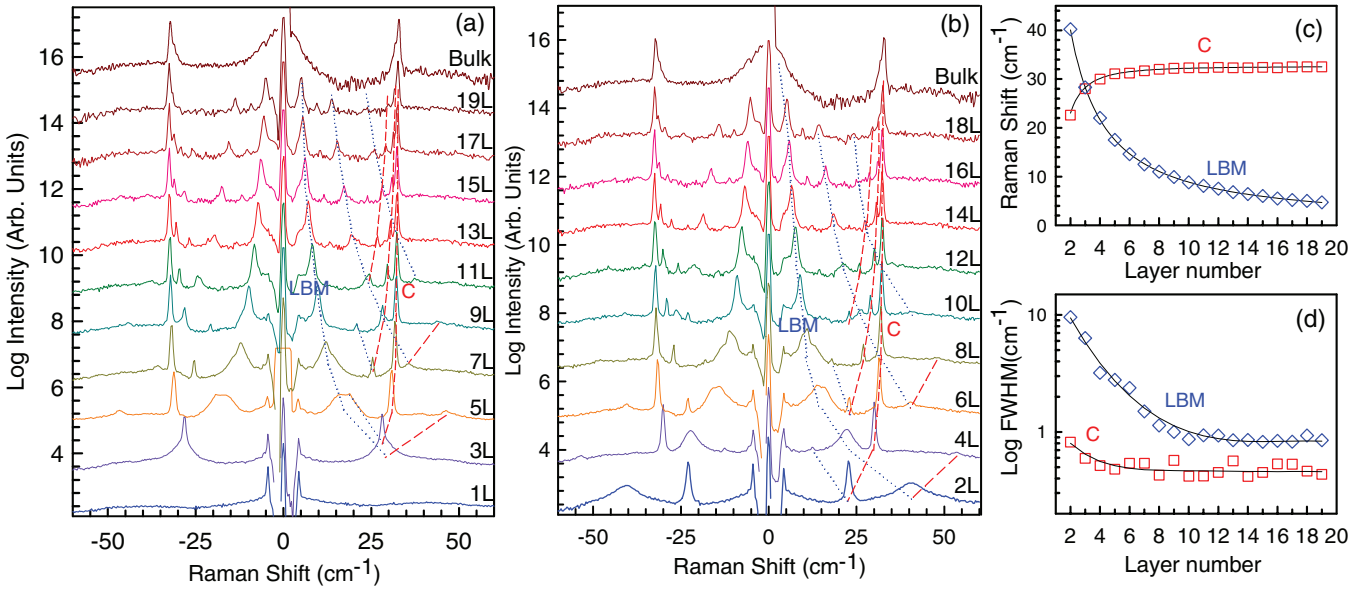

FIG. 3. (Color online) (a) Stokes and anti-Stokes Raman spectra of ONL-MoS_2 in the low-frequency range. (b) Stokes and anti-Stokes Raman spectra of ENL-MoS_2. The spectrum of bulk MoS_2 is also included in (a), (b). Dashed and dotted lines in (a), (b) are guides to the eye. (c) Position of typical C and LB modes as a function of N. (d) FWHM of C and LBM as a function of N. Solid lines in (c), (d) are guides to the eye.

We do not discuss the LBM (B^2_{2g}) in ENL-MoS_2 since it is Raman inactive. These tensors show that, in backscattering, the A'_1 modes in 5L-MoS_2 should appear only under unpolarized XX configuration, and E' should exist under both unpolarized XX and polarized YX configurations, while E'' should not appear for either XX or YX. Here YX indicates two mutually perpendicular axes within the basal plane of NL-MoS_2, the first being the polarization direction of the incident laser, the second the analyzer's polarization. For 6L-MoS_2 under backscattering, the E^2_{2g} modes exist for both XX and YX configurations.

In Fig. 2(b) two sharp peaks are observed under both XX and YX configurations at ~19 and ~30 cm^{-1} for 5L, and ~23 and ~32 cm^{-1} for 6L-MoS_2. According to the symmetry analysis discussed above, we assign these to E' in 5L and E^2_{2g} in 6L-MoS_2. Two broad peaks are observed for XX measurements at ~17 and 47 cm^{-1} for 5L-MoS_2, which we assign to A'_1. Note that the lower E' mode of 5L-MoS_2 at ~19 cm^{-1} cannot be fully resolved for XX measurements due to the presence of the broad A'_1 mode at ~17 cm^{-1}. We also detect two Raman modes at ~15 and 41 cm^{-1} in 6L-MoS_2. These are consistent with what should be optically silent B^2_{2g} LBMs, as discussed later. The symmetry, polarization, and mode frequency are summarized in Table I for the C and LB modes of 5 and 6L-MoS_2. Although the in-plane modes in 5 and 6L-MoS_2 above 200 cm^{-1} are almost identical, the C and LB mode positions below 100 cm^{-1} are different. The frequencies of all 5L-MoS_2 LBMs are higher than in 6L-MoS_2, while all C modes are lower than in 6L-MoS_2.

Figures 3(a) and 3(b) show the low-frequency Raman measurements for NL-MoS_2, with $N = 1$–19, as well as bulk MoS_2. Since the point group of ONL-MoS_2 (D_{3h}) is different from ENL-MoS_2 (D_{6h}), we plot the Raman spectra of ONL-MoS_2 [Fig. 3(a)] and ENL-MoS_2 [Fig. 3(b)] in two panels. Bulk MoS_2 is included both in ONL-MoS_2 and ENL-MoS_2 panels because we cannot distinguish its parity in a (noninfinite) bulk sample. Of course, there are no LB or C modes in 1L-MoS_2, as confirmed in Fig. 3(a). The two spikes ~4.55 cm^{-1}, with weaker intensity for thicker flakes, are due to Brillouin scattering of the LA mode from the Si substrate.[70] This is confirmed by determining the elastic constant C_{11} from $C_{11} = \rho v^2 \pi^2 / k_0^2 (\eta^2 + \kappa^2)$, where ρ is the Si density, v is the LA mode frequency, $k_0 = 2\pi/\lambda_0$, λ_0 is the incident light wavelength, and $(\eta + i\kappa)$ is the Si complex refractive index. The C_{11} determined from our Raman measurements (~1.65×10^{11} Pa) is consistent with 1.66×10^{11} Pa measured by ultrasonic wave propagation.[71] In 2L-MoS_2 two Raman peaks are observed, while two overlapping bands are seen in 3L-MoS_2. More Raman peaks are observed for thicker MoS_2 flakes.

We classify all low-frequency Raman peaks into two categories. Those that stiffen for increasing N, linked by dashed lines, and those softening with N, linked by dotted lines. One C mode stiffens from ~22.6 cm^{-1} in 2L to 32.5 cm^{-1} in 19L-MoS_2, while one LBM softens from ~40.1 cm^{-1} in 2L to 4.7 cm^{-1} in 19L-MoS_2, Fig. 3(c). The two sets of modes have different FWHM, Fig. 3(d). In 2L-MoS_2, FWHM

TABLE I. Symmetry, polarization, and positions of C and LB modes in 5 and 6L-MoS_2. The number (Num.) of each mode is indicated in the bracket before the mode.

		C		LBM	
5L	(Num.) mode	(2)E'(R,IR)	(2)E''(R)	(2)A'_1(R)	(2)A''_2(IR)
	polarization	XX,YX	XZ,YZ	XX	–
	exp. (cm^{-1})	19,30	–	17,47	–
6L	(Num.) mode	(3)E^2_{2g}(R)	(2)E_{1u}(IR)	(3)B^2_{2g}(silent)	(2)A_{2u}(IR)
	polarization	XX,YX	–	–	–
	exp. (cm^{-1})	23,32	–	15,41(XX)	–

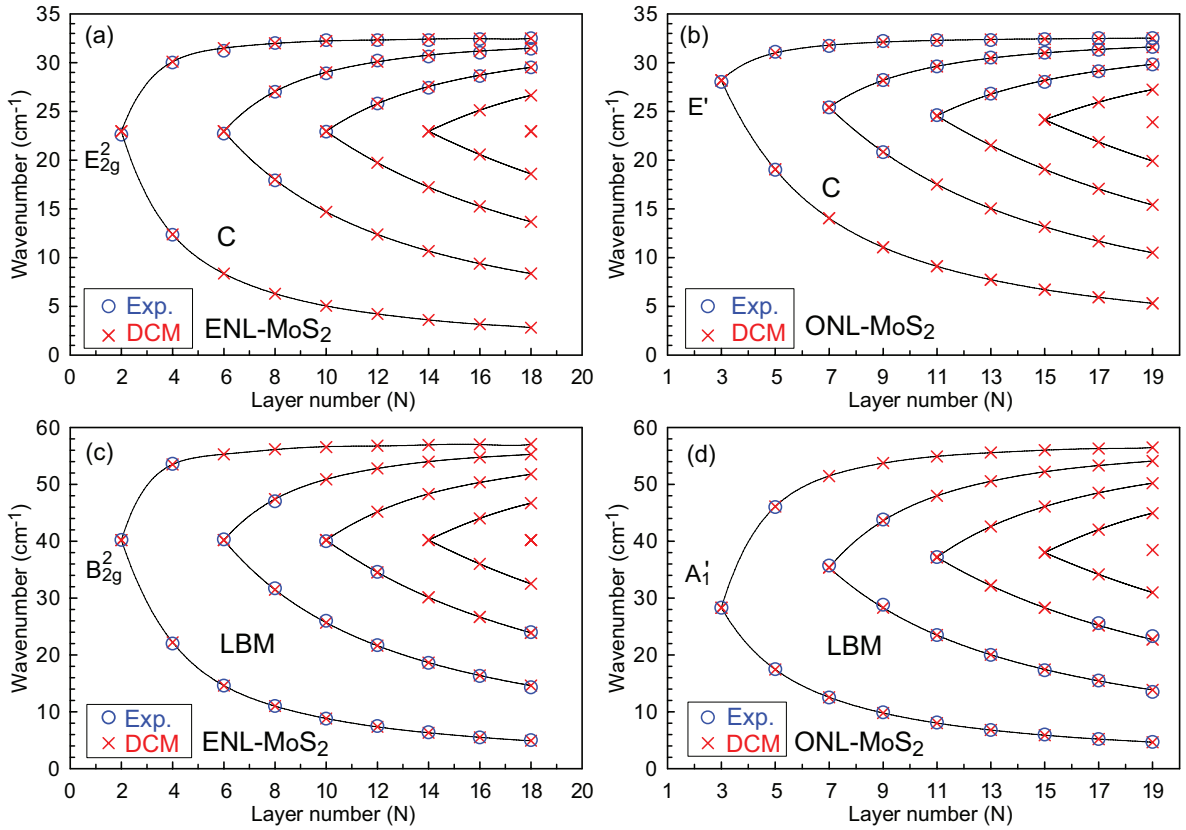

FIG. 4. (Color online) Position of C modes as a function of N for (a) ENL-MoS_2 and (b) ONL-MoS_2. Position of LBMs as a function of N for (c) ENL-MoS_2 and (d) ONL-MoS_2. The blue open circles are the experiment data. The red crosses are the diatomic chain model calculations. The irreducible representation of each mode is also indicated. Solid lines are guides to the eye.

(LBM ~40.1 cm^{-1}) is ~9.6 cm^{-1}, much larger than that (~0.8 cm^{-1}) of the C mode at 22.6 cm^{-1}. All data for ENL- and ONL-MoS_2 are summarized in Figs. 4(a)–4(d). According to group analysis, there should be no Raman active LBMs in ENL-MoS_2. However, a set of peaks are observed in ENL-MoS_2, with the same polarization behavior as LBMs in ONL-MoS_2, e.g., the two Raman modes ~15 and 41 cm^{-1} in 6L-MoS_2 in Fig. 2(b). Because their measured positions match well those predicted for LBMs, i.e., the B^2_{2g} modes in ENLs as discussed later, they are included in Fig. 4(c).

Since a MoS_2 layer consists of two types of atoms, S and Mo, we implement a diatomic chain model (DCM) to explain the data. Figure 1(a) shows the ball and stick model for 2 and 3L-MoS_2. Only two force constants are needed to describe the vibrations: α_{ss} and α_{sm}, where α_{ss} is the force constant per unit area between two nearest S planes in two adjacent layers, and α_{sm} is force constant per unit area between the nearest S and Mo planes within a MoS_2 layer. Their components perpendicular to the basal plane, $\alpha^{\perp}_{ss}$ and $\alpha^{\perp}_{sm}$, determine the LBMs lattice dynamics, while those parallel to the basal plane, $\alpha^{\parallel}_{ss}$ and $\alpha^{\parallel}_{sm}$, determine the C modes dynamics. The reduced mass for one S (Mo) plane, m_S (m_{Mo}), is its atomic mass per unit area. In MoS_2, $m_S = 0.6 \times 10^{-7}$ g/cm^2 and $m_{Mo} = 1.8 \times 10^{-7}$ g/cm^2. $\alpha^{\perp}_{sm}$ and $\alpha^{\parallel}_{sm}$ can be estimated from the high-frequency A'_1 and E' modes of 1L-MoS_2. In 1L-MoS_2, 9×9 dynamical matrices can be constructed and solved analytically. We get $\omega_{A'_1} = (1/2\pi c)\sqrt{2\alpha^{\perp}_{sm}/\mu}$, with $\mu = 2m_S$, and c the speed of light. The atom displacement eigenvectors show that the vibration directions of the two external S atoms are opposite along the c axis, while the center Mo atom stays still, as shown in Fig. 1(d) for 1L-MoS_2, corresponding to a spring connected by two S atoms with a force constant per unit area $2\alpha^{\perp}_{sm}$, since the Mo atom stays still at the spring equilibrium position. We measure $\omega_{A'_1}$ ~403 cm^{-1} in 1L-MoS_2. This gives $\alpha^{\perp}_{sm} = 3.46 \times 10^{21}$ N/m^3. We also get $\omega_{E'} = (1/2\pi c)\sqrt{2\alpha^{\parallel}_{sm}/\mu}$, where $1/\mu = 1/m_{Mo} + 1/(2m_S)$. The atom displacement eigenvectors indicate that the vibration directions of the two S atoms are opposite to the center Mo atom, along the basal plane, as shown in Fig. 1(d) for 1L-MoS_2, corresponding to a spring connected by two S atoms and one Mo atom with a force constant per unit area $2\alpha^{\parallel}_{sm}$. From the experimental 384 cm^{-1}, we get $\alpha^{\parallel}_{sm} = 1.88 \times 10^{21}$ N/m^3. Note that the weak interaction of the two S planes in the MoS_2 layers is not included because the S-S plane distance is twice the S-Mo one.

To understand the C modes of NL-MoS_2, the layer coupling between two nearest S planes in the two adjacent layers should be included. $3N \times 3N$ dynamical matrices can be constructed for NL-MoS_2. By numerically solving the eigenequation for NL-MoS_2, we get the eigenfrequencies and corresponding eigenvectors. By fitting these to our experimental data we get: $\alpha^{\perp}_{ss} = 8.90 \times 10^{19}$ N/m^3 and $\alpha^{\parallel}_{ss} = 2.82 \times 10^{19}$ N/m^3. Multiplying $\alpha^{\perp}_{ss}$ and $\alpha^{\parallel}_{ss}$ by the unit cell

area gives the interlayer force constants, $k_{ss}^{shear} = 2.5$ N/m and $k_{ss}^{LBM} = 7.8$ N/m. They agree well with those for bulk samples reported in Ref. 59 ($k_1^{shear} = 2.7$ N/m and $k_1^{comp} = 7.4$ N/m), derived by considering S-Mo-S as a rigid-layer mass unit, and deducing the interlayer force constants from $\omega = \sqrt{k_1/\mu_1}$, with ω the rigid-layer mode frequency and μ_1 the reduced mass. Multiplying $\alpha_{ss}^{\parallel}$ by the equilibrium distance between two adjacent MoS_2 layers gives a shear modulus ~18.9 GPa, in good agreement with that measured for bulk MoS_2,[72] from phonon dispersion curves determined by neutron scattering, and x-ray measurements of the linear compressibilities.

The eigenvectors of the rigid-layer vibrations in 2 and 3L-MoS_2, derived from the corresponding eigenequations, are depicted in Figs. 1(b) and 1(c). Applying symmetry analysis to the corresponding NL-MoS_2 eigenvectors, we assign the irreducible representations of the corresponding point group to each mode. The eigenfrequencies of Raman active rigid-layer vibrations for E_{2g}^2 (C modes in ENL-MoS_2), E' (C modes in ONL-MoS_2), and A_1' (LBMs in ONL-MoS_2) are summarized in Figs. 4(a), 4(b), and 4(d). The eigenfrequencies of the Raman inactive B_{2g}^2 (LBMs) in ENL-MoS_2 are also included in Fig. 4(c). The eigenfrequencies of the modes for 1L-, 2L-, and 3L-MoS_2 are also given in Figs. 1(b)–1(d). As illustrated in Fig. 4, the model calculations are in good agreement with experiments, including the Raman inactive B_{2g}^2. This suggests that the Raman inactive LBMs (B_{2g}^2) in ENL-MoS_2 might be observed, with polarization behavior identical to the A_1' (LBMs) in ONL-MoS_2.

We now consider the evolution of the rigid-layer vibrations with increasing N based on symmetry analysis. In Figs. 4(a) and 4(c), one C mode (E_{2g}^2) and one LBM (B_{2g}^2) are observed in 2L-MoS_2. Each splits in two branches with increasing N, one stiffening, the other softening with N. A new mode appears when N increases up to $4N + 2$, $N = 1,2,3,\ldots$, and splits into two branches again for higher N. The C modes (E') [Fig. 4(b)] and LBMs (A_1') [Fig. 4(d)] in ONL-MoS_2 exhibit similar trends with N as the C modes (E_{2g}^2) [Fig. 4(a)] and LBMs (B_{2g}^2) [Fig. 4(c)] in ENL-MoS_2, but with decreasing frequency for E' and increasing frequency for A_1'. Connecting each branch of the rigid-layer modes with solid lines shows that these form series of cone-like curves, Figs. 4(a)–4(d). The number of LB and shear modes in ONL- and ENL-MoS_2 increases with N. However, in the experiment, no more than three of them are observed. In both ONL- and ENL-MoS_2, most of the observed shear modes are from the upper branch and their frequencies stiffen with increasing N, while most of the LBMs are from the lower branch, and their frequencies soften with increasing N.

Figure 5 plots the positions of all the observed and calculated rigid-layer vibration modes. The shear mode at 22.6 cm^{-1} (E_{2g}^2) in 2L-MoS_2 blue-shifts to 28 cm^{-1} (E') in 3L-MoS_2, and to 32.5 cm^{-1} (E') in 19L-MoS_2, reaching ~32.7 cm^{-1} (E_{2g}^2) in bulk MoS_2. In multilayer graphene,[40] with each layer composed of one type of atom, the ratio of C peak positions in bulk and bilayer graphene (2LG) is $\omega_{bulk}/\omega_{2LG} = \sqrt{2}$. In our MoS_2 measurements, the shear mode exhibits the same trend and we have $32.7/22.6 = 1.447$, very close to $\sqrt{2}$. On the other hand, the LBM at 40 cm^{-1} (B_{2g}^2) in

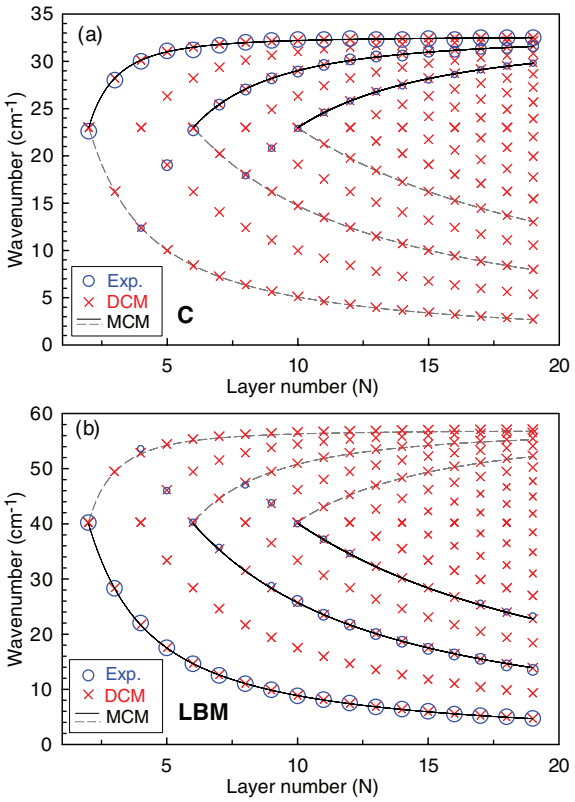

FIG. 5. (Color online) Position of (a) C modes and (b) LBMs as a function of N. The blue open circles are the experimental data. The diameter of the circles represents the Raman intensity of each mode. The red crosses are calculations based on the diatomic chain model (DCM). The black solid lines in (a) and (b) are, respectively, fitted by $\omega_C(N) = \omega_C(2)\sqrt{1 + cos(N_0\pi/N)}$ ($N \geqslant 2N_0$) and $\omega_{LBM}(N) = \omega_{LBM}(2)\sqrt{1 - cos(N_0\pi/N)}$ ($N \geqslant 2N_0$) for the phonon branches originating from 2L-($N_0 = 1$), 6L-($N_0 = 3$) and 10L($N_0 = 5$)-MoS_2 based on the monatomic chain model (MCM). The gray dashed lines are another set of the C and LB modes based on the MCM.

2L red-shifts to 29 cm^{-1} (A_1') in 3L-MoS_2, and 5 cm^{-1} (A_1') in 19L-MoS_2. The blue-shifted branch reaches 56.8 cm^{-1} in 19L-MoS_2, close to the LBM value in bulk MoS_2.[73]

For C and LB modes in NL-MoS_2, three atoms of the S-Mo-S layer vibrate along same direction, as shown in Figs. 2(b) and 2(c). Based on our DCM, we find that the relative displacements between Mo and two S atoms are very small. For example, the relative displacement in 2L-MoS_2 is ~0.6%, decreasing with increasing N. Therefore, the relative vibration of C and LB modes between Mo and two S atoms can be ignored. We can thus further simplify the model collapsing an entire layer in a single ball. So we consider a reduced monatomic chain model (MCM). Taking one layer as a ball with mass ($m_{Mo} + 2m_s$) and interlayer bonding $\alpha_{ss}^{\perp}$ for LBMs, and $\alpha_{ss}^{\parallel}$ for C modes, we get: $\omega_{LBM} = (1/\sqrt{2}\pi c)\sqrt{\alpha_{ss}^{\perp}/(m_{Mo} + 2m_s)}$, $\omega_C = (1/\sqrt{2}\pi c)\sqrt{\alpha_{ss}^{\parallel}/(m_{Mo} + 2m_s)}$ for 2L-MoS_2, with ω_{LBM} the LBM position, and ω_C the C peak position. The corresponding ω_{LBM} (40.8 cm^{-1}) and ω_C (23.0 cm^{-1}) are in good agreement

with those from the DCM ($\omega_{LBM} = 40.3\,cm^{-1}$ and $\omega_C = 22.9\,cm^{-1}$) and the experimental data ($\omega_{LBM} = 40.2\,cm^{-1}$ and $\omega_C = 22.6\,cm^{-1}$). We can now solve the eigenequation analytically and find the relation between position and N both for shear and LB modes. These modes can be assigned to several branches, as shown in Fig. 5. A new branch will emerge from each ENL-MoS_2, i.e., 2,4,6,8L, . . .-MoS_2, at about the same position as that of the C mode or LBM in 2L-MoS_2, then splitting into two sub-branches, one blue shifting, the other red shifting with increasing N. For the branches originating from each ENL-MoS_2, the frequency as a function of N is $\omega(N) = \omega(2N_0)\sqrt{1 \pm \cos(N_0\pi/N)}$ ($N \geqslant 2N_0$, and N_0 an integer: 1,2,3,4 . . . .), with + for the high-frequency subbranch and − for the low-frequency one. Our calculations show that $\omega(2N_0)$ is almost the same as $\omega(2)$ both for C and LB modes. Therefore, the evolution of C and LB modes with increasing N can be further simplified as $\omega(N) = \omega(2)\sqrt{1 \pm \cos(N_0\pi/N)}$ ($N \geqslant 2N_0$, and N_0 an integer: 1,2,3,4 . . . .).

For NL-MoS_2 the observed C modes are usually in the high-frequency subbranch, while the corresponding LBMs are usually in the low-frequency one; these are connected by solid lines in Fig. 5. The appearance of the high-frequency C subbranches and the absence of the high-frequency LBM subbranches is consistent with the bulk case, where the C mode E^2_{2g} is Raman-active while the LBM B^2_{2g} is optical-inactive. For the observed high-frequency C subbranch originating from 2L-MoS_2, we have $N_0 = 1$, thus $\omega_C(N) = \omega_C(2)\sqrt{1 + \cos(\pi/N)}$ ($N \geqslant 2$), where $\omega_C(2) = 23.0\ cm^{-1}$. If we replace $\omega_C(2) \sim 23.0\ cm^{-1}$ in MoS_2 with $\omega_C(2) \sim 31\ cm^{-1}$, this relation describes the C peaks in multilayer graphene.[40] Similarly, $\omega_C(N) = \omega_C(2)\sqrt{1 + \cos(3\pi/N)}$ ($N \geqslant 6$) for the high-frequency subbranch originating from 6L-MoS_2, and $\omega_C(N) = \omega_C(2)\sqrt{1 + \cos(5\pi/N)}$ ($N \geqslant 10$) for the high-frequency subbranch originating from 10L-MoS_2. For the observed LBMs in MoS_2, the relation between frequency and N in the low-frequency subbranch originating from 2, 6 and 10L-MoS_2 is: $\omega_{LBM}(N) = \omega_{LBM}(2)\sqrt{1 - \cos(i * \pi/N)}$ ($N \geqslant 2 * i$), $i = 1,3,5$, where $\omega_{LBM}(2) = 40.8\ cm^{-1}$. This well matches with the experiments, Figs. 5(a) and 5(b). Figure 5 also shows another sub-branch for 2, 6, and 10L-MoS_2, both for C and LB modes, as indicated by gray dashed lines. Only one or two modes are experimentally observed for these sub-branches. Their frequency is in good agreement with the theoretical prediction.

Note that any coupling between supported MoS_2 and the substrate is not included in our chain models. The agreement between experiments and model predictions means that the coupling between MoS_2 and the substrate does not play a major role, the scaling with N being only determined by the interaction between the MoS_2 layers. Indeed, for the suspended multilayer graphene in Ref. 40, no coupling was considered, and the C scaling with N was also well described by a MCM.

In principle, our chain model can be extended to predict rigid-layer vibrations in other LMs. The general approach is to calculate the reduced mass for the monolayer of a given material, and then measure C and LBMs in 2L samples. One can then predict the relation between frequency and N for the different branches in any LM. For example, the theoretical positions of the C and LB modes in 2L-hBN are ∼38.6 cm^{-1} and 85.6 cm^{-1}, respectively.[57] Our model predicts that the C mode generates two branches, $\omega_C(N) = 38.6\sqrt{1 + \cos(\pi/N)}$ ($N \geqslant 2$) at higher frequency, and $\omega_C(N) = 38.6\sqrt{1 - \cos(\pi/N)}$ ($N \geqslant 2$) at lower. The LBM also generates two branches, $\omega_{LBM}(N) = 85.6\sqrt{1 + \cos(\pi/N)}$ ($N \geqslant 2$) at higher frequency, and $\omega_{LBM}(N) = 85.6\sqrt{1 - \cos(\pi/N)}$ ($N \geqslant 2$) at lower. Similarly, the C mode (∼38.6 cm^{-1}) and LBM (∼85.6 cm^{-1}) in 4L-hBN, will also generate two branches, and so on. Thus, we can predict all the C and LB modes in NL-hBN.

III. CONCLUSIONS

We characterized single- and few-layer MoS_2 by Raman spectroscopy. We observed rigid-layer vibrations both for shear and layer breathing modes. These were assigned to irreducible representations of the point group that the sample belongs to, as confirmed by polarized Raman spectroscopy. These change with number of layers, with different scaling for odd and even layers. A diatomic chain model, combined with group theory, can account for the observed trends. Furthermore, a reduced monatomic chain model can be used to describe the shear and layer breathing modes in MoS_2 and any other layered material with any number of layers.

ACKNOWLEDGMENTS

We acknowledge support from the special funds for Major State Basic Research of China, Contract No. 2009CB929301, the National Natural Science Foundation of China, Grants No. 11225421 and No. 10934007, EU grants NANOPOTS and GENIUS, EPSRC Grants No. EP/K01711X/1, No. EP/K017144/1, and a Royal Society Wolfson Research Merit Award.

*acf26@eng.cam.ac.uk
†phtan@semi.ac.cn

[1] K. S. Novoselov and A. H. Castro Neto, Phys. Scr., T **146**, 014006 (2012).
[2] F. Bonaccorso, A. Lombardo, T. Hasan, Z. Sun, L. Colombo, and A. C. Ferrari, Mater. Today **15**, 564 (2012).
[3] J. N. Coleman *et al.*, Science **331**, 568 (2011).
[4] J. A. Wilson and A. D. Yoffe, Adv. Phys. **18**, 193 (1969).
[5] P. Poizot, S. Laruelle, S. Grugeon, L. Dupont, and J. M. Tarascon, Nature (London) **407**, 496 (2000).
[6] S. V. Prasad and J. S. Zabinski, Nature (London) **387**, 761 (1997).
[7] H. D. Abruna and A. J. Bard, J. Electrochem. Soc. **129**, 673 (1982).
[8] R. F. Frindt, J. App. Phys. **37**, 1928 (1966).
[9] R. P. Clement, Inorg. Chem. **17**, 2754 (1978).
[10] G. L. Frey, K. J. Reynolds, R. H. Friend, H. Cohen, and Y. Feldman, J. Am. Chem. Soc. **125**, 5998 (2003).
[11] S. K. Mishrayz, S. Satpathyyz, and O. Jepsenz, J. Phys.: Condens. Matter **9**, 461 (1997).
[12] C. L. Kane and E. J. Mele, Phys. Rev. Lett. **95**, 226801 (2005).

[13]B. Radisavljevic, A. Radenovic, J. Brivio, V. Giacometti, and A. Kis, Nature Nanotech. **6**, 147 (2011).
[14]K. F. Mak, C. Lee, J. Hone, J. Shan, and T. F. Heinz, Phys. Rev. Lett. **105**, 136805 (2010).
[15]A. Splendiani, L. Sun, Y. Zhang, T. Li, J. Kim, C. Y. Chim, G. Galli, and F. Wang, Nano Lett. **10**, 1271 (2010).
[16]R. S. Sundaram, M. Engel, A. Lombardo, R. Krupke, A. C. Ferrari, P. Avouris, and M. Steiner, arXiv:1211.4311.
[17]K. F. Mak, K. He, J. Shan, and T. F. Heinz, Nature Nanotech. **7**, 494 (2012).
[18]H. Zeng, J. Dai, W. Yao, D. Xiao, and X. Cui, Nature Nanotech. **7**, 490 (2012).
[19]T. Cao *et al*., Nature Commun. **3**, 887 (2012).
[20]T. Böker, R. Severin, A. Müller, C. Janowitz, R. Manzke, D. Voß, P. Krüger, A. Mazur, and J. Pollmann, Phys. Rev. B **64**, 235305 (2001).
[21]R. Coehoorn, C. Haas, J. Dijkstra, C. J. F. Flipse, R. A. de Groot, and A. Wold, Phys. Rev. B **35**, 6195 (1987).
[22]R. Coehoorn, C. Haas, and R. A. de Groot, Phys. Rev. B **35**, 6203 (1987).
[23]L. F. Mattheiss, Phys. Rev. B **8**, 3719 (1973).
[24]Y. Kim, J.-L. Huang, and C. M. Lieber, Appl. Phys. Lett. **59**, 3404 (1991).
[25]K. S. Novoselov, Science **306**, 666 (2004).
[26]K. K. Kam and B. A. Parkinson, J. Phys. Chem. **86**, 463 (1982).
[27]T. Li and G. Galli, J. Phys. Chem. C **111**, 16192 (2007).
[28]Y. Zhang, J. Ye, Y. Matsuhashi, and Y. Iwasa, Nano Lett. **12**, 1136 (2012).
[29]H. Liu and P. D. Ye, IEEE Electron Dev. Lett. **33**, 546 (2012).
[30]H. Liu, A. T. Neal, and P. D. Ye, ACS Nano **6**, 8563 (2012).
[31]Z. Yin, H. Li, H. Li, L. Jiang, Y. Shi, Y. Sun, G. Lu, Q. Zhang, X. Chen, and H. Zhang, ACS Nano **6**, 74 (2012).
[32]S. Alkis, T. Özta, L. E. Aygün, F. Bozkurt, A. K. Okyay, and B. Ortaç, Opt. Express. **20**, 21815 (2012).
[33]H. S. Lee, S. W. Min, Y. G. Chang, M. K. Park, T. Nam, H. Kim, J. H. Kim, S. Ryu, and S. Im, Nano Lett. **12**, 3695 (2012).
[34]A. C. Ferrari and J. Robertson, Philos. Trans. R. Soc. Lond. A **362**, 2477 (2004).
[35]A. C. Ferrari, Solid State Commun. **143**, 47 (2007).
[36]F. Tuinstra and J. L. Koenig, J. Chem. Phys. **53**, 1126 (1979).
[37]R. J. Nemanich and S. A. Solin, Phys. Rev. B **20**, 392 (1979).
[38]W. Yan, D. C. Alsmeyer, and R. L. McCeery, Chem. Mater. **2**, 557 (1990).
[39]A. C. Ferrari *et al*., Phys. Rev. Lett. **97**, 187401 (2006).
[40]P. H. Tan *et al*., Nature Mater. **11**, 294 (2012).
[41]C. H. Lui, L. M. Malard, S. Kim, G. Lantz, F. E. Laverge, R. Saito, and T. F. Heinz, Nano Lett. **12**, 5539 (2012).
[42]C. H. Lui and T. F. Heinz, arXiv:1210.0960 [Phys. Rev. B (to be published)].
[43]K. Sato, J. S. Park, R. Saito, C. Cong, T. Yu, C. H. Lui, T. F. Heinz, G. Dresselhaus, and M. S. Dresselhaus, Phys. Rev. B **84**, 035419 (2011).
[44]S. Latil, V. Meunier, and L. Henrard, Phys. Rev. B **76**, 201402(R) (2007).
[45]E. McCann, Phys. Rev. B **74**, 161403(R) (2006).
[46]M. Koshino and T. Ando, Solid State Commun. **149**, 1123 (2009).
[47]T. Sekine, T. Nakashizu, K. Toyoda, K. Uchinokura, and E. Matsuura, Solid State Commun. **35**, 371 (1980).
[48]S. Reich, A. C. Ferrari, R. Arenal, A. Loiseau, I. Bello, and J. Robertson, Phys. Rev. B **71**, 205201 (2005).
[49]C. Lee, H. Yan, L. E. Brus, T. F. Heinz, J. Hone, and S. Ryu, ACS Nano **4**, 2695 (2010).
[50]J. Zhang, Z. Peng, A. Soni, Y. Zhao, Y. Xiong, B. Peng, J. Wang, M. S. Dresselhaus, and Q. Xiong, Nano Lett. **11**, 2407 (2011).
[51]G. Plechinger, S. Heydrich, J. Eroms, D. Weiss, C. Schueller, and T. Korn, Appl. Phys. Lett. **101**, 101906 (2012).
[52]H. Zeng, B. Zhu, K. Liu, J. Fan, X. Cui, and Q. M. Zhang, Phys. Rev. B **86**, 241301(R) (2012).
[53]J. L. Verble and T. J. Wieting, Phys. Rev. Lett. **25**, 362 (1970).
[54]T. J. Wieting and J. L. Verble, Phys. Rev. B **3**, 4286 (1971).
[55]H. Li, Q. Zhang, C. C. Ray Yap, B. K. Tay, T. H. T. Edwin, A. Olivier, and D. Baillargeat, Adv. Funct. Mater. **22**, 1385 (2012).
[56]T. Kuzuba and M. Ishii, Phys. Status Solidi B **155**, K13 (1989).
[57]K. H. Michel and B. Verberck, Phys. Rev. B **85**, 094303 (2012).
[58]A. Molina-Sanchez and L. Wirtz, Phys. Rev. B **84**, 155413 (2011).
[59]R. Zallen and M. Slade, Phys. Rev. B **9**, 1627 (1974).
[60]N. S. Luo, P. Ruggerone, and J. P. Toennies, Phys. Rev. B **54**, 5051 (1996).
[61]K. S. Novoselov, A. K. Geim, S. V. Morozov, D. Jiang, M. I. Katsnelson, I. V. Grigorieva, S. V. Dubonos, and A. A. Firsov, Nature (London) **438**, 197 (2005).
[62]C. Casiraghi, A. Hartschuh, E. Lidorikis, H. Qian, H. Harutyunyan, T. Gokus, K. S. Novoselov, and A. C. Ferrari, Nano Lett. **7**, 2711 (2007).
[63]S. Jimenez Sandoval, D. Yang, R. F. Frindt, and J. C. Irwin, Phys. Rev. B **44**, 3955 (1991).
[64]G. Y. Zhang, G. X. Lan, and Y. F. Wang, *Lattice Vibration Spectroscopy*, 2nd ed. (High Education Press, China, 1991).
[65]C. Ataca, M. Topsakal, E. Aktürk, and S. Ciraci, J. Phys. Chem. C **115**, 16354 (2011).
[66]P. N. Ghosh and C. R. Maiti, Phys. Rev. B **28**, 2237 (1983).
[67]B. C. Windom, W. G. Sawyer, and D. W. Hahn, Tribol. Lett. **3**, 301 (2011).
[68]R. Loudon, Adv. Phys. **50**, 813 (2001).
[69]O. D. Dumcenco, Y. C. Su, Y. P. Wang, K. Y. Chen, Y. S. Huang, C. H. Ho, and K. K. Tiong, Chinese J. Phys. **49**, 270 (2011).
[70]M. H. Kuok, S. C. Ng, Z. L. Rang, and D. J. Lockwood, Phys. Rev. B **62**, 12902 (2000).
[71]H. J. McSkimin and P. Andreatch, J. Appl. Phys. **35**, 2161 (1964).
[72]J. L. Feldman, J. Phys. Chem. Solids **42**, 1029 (1981).
[73]N. Wakabayashi, H. G. Smith, and R. M. Nicklow, Bull. Am. Phys. Soc. **17**, 292 (1972).